Nuclear Instruments and Methods in Physics Research A 833 (2016) 169–180

Contents lists available at ScienceDirect

Nuclear Instruments and Methods in Physics Research A

journal homepage: www.elsevier.com/locate/nima

Front-end electronics for the Muon Portal project

S. Garozzo [a,*], D. Marano [a], G. Bonanno [a], A. Grillo [a], G. Romeo [a], M.C. Timpanaro [a], D. Lo Presti [b], F. Riggi [b], V. Russo [b], D. Bonanno [b], P. La Rocca [b], F. Longhitano [b], D.G. Bongiovanni [b], G. Fallica [c], G. Valvo [c]

[a] INAF, Osservatorio Astrofisico di Catania, Via S. Sofia 78, I-95123 Catania, Italy
[b] Università di Catania, Dipartimento di Fisica e Astronomia, and INFN, Sezione di Catania, Via S. Sofia 64, I-95123 Catania, Italy
[c] ST-Microelectronics, Stradale V Primosole 50, Catania, Italy

ARTICLE INFO

Article history:
Received 4 April 2016
Received in revised form
31 May 2016
Accepted 4 July 2016
Available online 7 July 2016

Keywords:
Cosmic rays
Front-end electronics
Muon tomography
Remote control
Scintillation detectors
Silicon photomultipliers

ABSTRACT

The Muon Portal Project was born as a joint initiative between Italian research and industrial partners, aimed at the construction of a real-size working detector prototype to inspect the content of traveling containers by means of secondary cosmic-ray muon radiation and recognize potentially dangerous hidden materials. The tomographic image is obtained by reconstructing the incoming and outgoing muon trajectories when crossing the inspected volume, employing two tracker planes located above and below the container under inspection. In this paper, the design and development of the front-end electronics of the Muon Portal detector is presented, with particular emphasis being devoted to the photo-sensor devices detecting the scintillation light and to the read-out circuitry which is in charge of processing and digitizing the analog pulse signals. In addition, the remote control system, mechanical housing, and thermal cooling system of all structural blocks of the Muon Portal tracker are also discussed, demonstrating the effectiveness and functionality of the adopted design.

1. Introduction

In line with the increasing demand for selected security controls at ports and boards, novel advanced technologies offering improved detection of hidden nuclear materials and special weapons have been recently given considerable research attention to thwart nuclear proliferation and terrorism throughout the world. The annual traffic of vehicles and containers transporting persons and materials is constantly growing over time; however, effective inspection protocols are currently applied to exiguous percentages of the overall worldwide traveling platforms, owing to the prohibitive time-consuming procedures and remarkable costs required.

In order to avoid manual inspection of freight, cargo and shipping containers, numerous radiation detection techniques have been developed for identifying the presence of nuclear elements emitting radiations. The most commonly adopted approach relies on the X-ray absorption from an intense external source; alternative techniques, such as directional gamma-ray imaging and neutron radiography, have also been considered. However, these strategies have not been proven to be particularly sensitive to heavily shielded nuclear materials, because of radiation absorption phenomena, and entail the release of additional radiation levels into the natural environment.

To keep pace with the emerging demand for more rigorous safety standards and regulations, requiring the inspection of all transiting containers, advanced non-intrusive scanning instruments have been developed over the last few years to detect dense materials which might be consistent in presence of particular fissile elements [1–3]. In this context, cosmic muon tomography is one of the most promising technique, exploiting the scattering process of secondary cosmic radiation at the sea level, which is particularly sensitive to the atomic number Z of the traversed material. From the determination of the muon angular deviation induced by heavy materials when crossing the particle tracker, a three-dimensional (3D) map of the scattering points can be truthfully reconstructed, detecting any hidden high-Z fissile sample (i.e. U, Pu) or shielding (i.e. Pb) in a reasonable amount of time. Compared to traditional inspection methods, muon tomography benefits from a non-invasive scan operation, provides a reliable 3D density profile of the inspected volume, and prevents additional harmful radiation from contaminating the atmosphere. In light of the above features, muon tomography enhances the existing radiation detection portals, allowing an accurate screening of containers in short acquisition times, complying with the general requirement of a fast inspection technique [4–7].

Different projects have been proposed worldwide in recent

* Corresponding author.

http://dx.doi.org/10.1016/j.nima.2016.07.009
0168-9002/

years, with the target of constructing prototype detectors for muon tomography. Within this framework, the Muon Portal Collaboration (endorsed by a few local research institutions and industrial companies) recently undertook a new innovative project aiming at the development of a real-size tomographic prototype detector (18-m^2 sensitive area for each of the 4 logical planes), specifically designed for the identification and localization of potentially dangerous materials inside standard traveling containers [8–17]. A considerable amount of simulations and tests with different reconstruction and visualization algorithms has demonstrated the feasibility of the project, enabling the possibility of gaining sufficient information in short acquisition windows to reconstruct the tomographic image with the required precision and resolution [13–17].

Two main considerations about the expected integration time in the proposed Muon Portal project should be taken into account. First, in a reasonable amount of time, about ten minutes, the system must take the decision if an accurate inspection is needed; this is the case of a container in which the number of scattered muon tracks exceeds a prefixed threshold level. A longer duration of the preliminary inspection could paralyze the flux of containers through the control gates. Second, once a preliminary alert signal has been given, the suspected container can be cleared if, after about one day long data acquisition, no evidence of a high-density object bigger than 1 dm^3 has been detected. The optimal time windows for the fulfillment of these two constraints will be chosen by data analysis after a measurement campaign in the final conditions of detector size.

After an extensive R&D phase, which led to the choice and test of the individual components, the Muon Portal Project has entered the construction phase, and the installation of the detection modules is almost completed.

This paper reports on the design and development of the front-end electronics of the Muon Portal detector, from the photo-sensor devices adopted to detect the photons emitted by the scintillation light, to the read-out circuits dedicated to process and digitize the output analog pulses, also including the remote control system for the acquisition and monitoring of voltages and temperatures of all functional blocks of the detector tracker.

Following this introduction, the remainder of the paper is organized as follows. A technical description of the detector tracker is briefly addressed in Section 2. Section 3 details the front-end electronics of the Muon Portal detector, discussing the used photo-sensors and related front-end read-out. The remote control system of the tracking detector is described in Section 4. Section 5 reports on the mechanical housing and cooling system. Finally, Section 6 draws the authors' conclusions.

2. The Muon Portal detector

The structure of the Muon Portal detector consists of 8 position-sensitive physical planes, corresponding to 4 logical XY planes of 3×6-m^2 each, two placed above and two below the container volume to be investigated, as schematically sketched in Fig. 1. Due to the envisaged distance between the detection planes (1.4 m) and the inner part of the detector (2.8 m in height), a spatial resolution on the order of a few millimeters is required for all planes, in order to provide good tracking capabilities for the entering charged particles, reconstruct their incoming and outgoing trajectories, and evaluate the amount of scattering suffered by each track. The overall size of the detector is suitable for a full inspection of a real TEU (Twenty-foot Equivalent units) container.

For a feasible implementation of the set-up, the baseline layout of the detector architecture is derived from a modular-type design approach. In fact, each physical plane is composed of 6 functional

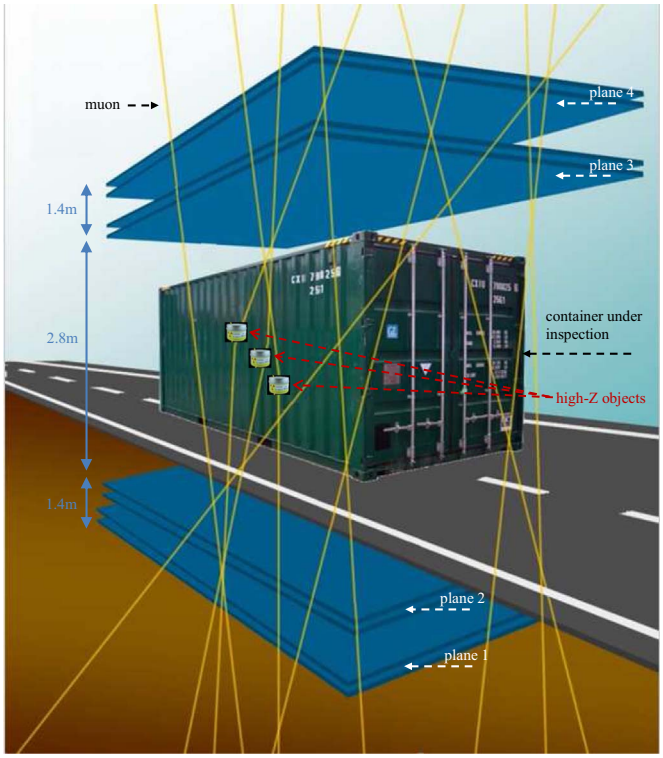

Fig. 1. Artist's view of the Muon Portal detector layout, illustrating the detection of high-Z objects inside a container. Two XY logical planes are placed above and below the container, in order to reconstruct the muon tracks before and after traversing the container volume, in search of muon scattering from high-Z materials.

modules (1 m $\times$ 3 m) covering either the X- or the Y-coordinates in a proper geometry so as to minimize the dead area, estimated in the order of 0.1% of the total sensitive area. As a result, 48 structural modules are required for the 8 physical planes of the detector.

Each detection module is segmented in 100 strips ($1 \times 1 \times 300$ cm^3) of extruded plastic scintillator. Two Wave-Length-Shifting fibers (WLS), Kurary[1] Y-11 (200) MJ, 1 mm round section, are placed on each strip to convey the light engendered by the crossing particles, and are both optically and mechanically coupled to suitable photo-sensors, positioned at one of the fiber extremities, which convert the scintillating light into electrical pulse signals. Fig. 2 pictorially illustrates the structural arrangement of the 12 basic modules (denominated M1-M12) in each of the 4 logical planes. The choice of extruded plastic scintillator strips for cosmic muon detection is based on a reasonable trade-off in terms of efficiency, light yield, emission, absorption spectra, costs and availability.

The detection planes are supported by a customized mechanical structure, with the aim of providing a suitable sustenance for the detector planes and minimizing the amount of material budget traversed by the charged particles. The mechanical structure is made by 6 supports in iron steel of a few centimeters thickness, with a light metal grid for each tracking plane.

3. Front-end electronics

The front-end electronics of the Muon Portal tracker, hereafter described, includes the photo-sensor devices detecting the light generated by the crossing muons, as well as the read-out circuits

[1] http://kuraraypsf.jp/psf/ws.html.

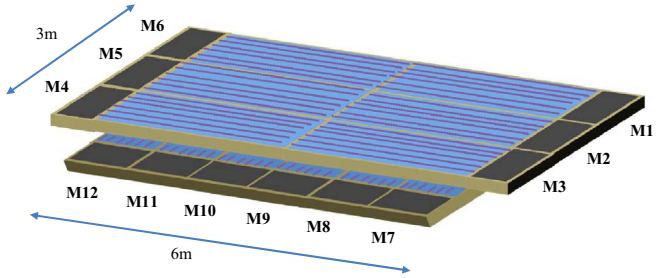

Fig. 2. Pictorial representation of an XY logical plane, consisting of 12 functional modules (M1-M12). The 200 optical fibers in each module are terminated on the photo-sensors devices and related front-end electronics.

conditioning and processing the analog pulses and converting them into digital signals.

3.1. SiPM photo-sensors

The read-out of the scintillation light produced in the strips and transported by the WLS fibers relies on silicon photomultiplier (SiPM) sensors, a rapidly-developing class of solid-state detectors which have been recently gaining great interest and extensive diffusion in the fields of high-energy physics, nuclear medicine, and astrophysics [18–26].

The photosensors used in the Muon Portal detector requires an appropriate design to be adapted to the mechanical requirements and to the optical properties of the strips and the WLS fibers. SiPMs allows to fit the size of the used fibers and match their emission spectrum. In addition, the selected WLS fibers to transport the light produced in the scintillating strips greatly reduce the light absorption along the strip and enables to adapt the wavelength of the emitted light to the spectral region of the SiPM maximal sensitivity.

The SiPM prototype devices realized for the Muon Portal project are custom-designed detectors, fabricated by ST-Microelectronics (STM), aimed at maximizing the photon detection efficiency (*PDE*), ensuring relatively low dark count rate (*DCR*) and optical cross-talk values. Numerous preliminary characterization activities were carried out in terms of both electrical and optical performance parameters, in order to select the optimal SiPM devices, for a given temperature and operating condition, before the mass production. The final monolithic chip is based on an *n-on-p* technology and embeds 4 individual round-shaped SiPMs, as shown on the micro-photographs of Fig. 3.

The monolithic chip ($\sim 5 \times 5$ mm^2) integrates two types of SiPMs of equal physical dimensions, which differ only for their cell pitch: the MUON-60 device features 548 microcells with 60-μm pitch, while the MUON-75 SiPM is constituted by 320 cells with a

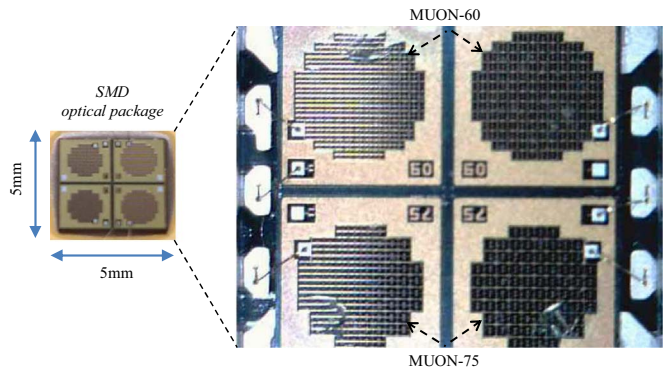

Fig. 3. Microphotograph of the SiPM chip employed for the Muon Portal detector (upper row: MUON-60; lower row: MUON-75).

Table 1
Main physical features of the SiPM detectors employed in the front-end electronics (MUON-60 by ST-Microelectronics).

Parameter	Value
Device size	2.09 mm × 2.09 mm
Cell pitch	60 μm × 60 μm
Sensitive area	1.97 mm^2
Micro-pixels	548
Cell fill-factor	67.4%
Breakdown voltage[a]	26.9 V – 27.7 V

[a] Among the 9600 devices used, evaluated at room temperature (25 °C).

75-μm pitch. The SiPM size is circular with a diameter of about 1.5 mm, and the distance between the centers of the two SiPMs is chosen to optimize coupling with fibers. Along with the standard contacts for the anode and cathode electrodes, both SiPM types are provided with a third additional pad connected to an independent photodiode microcell, allowing for a more accurate breakdown voltage estimation. The SiPM type being considered for the Muon Portal application is the MUON-60 detector, due to the much reduced DCR and optical cross-talk compared to the MUON-75 counterpart. The main physical characteristics of the MUON-60 SiPM, provided by the manufacturer, are summarized in Table 1, along with the measured spread in the breakdown voltages among all the tested devices.

Extensive electro-optical characterization of the MUON-60 SiPMs is performed with the set-up described in [22,23], in order to assess the main performance parameters and sort out the devices according to their breakdown voltages and equalize the gain of different SiPMs installed in the same region of the detector [12].

Dedicated mechanical supports (cookies) placed at one end of the strips allow to route and align the WLS fibers, which are then polished and finally coupled to the SiPM chips and are enclosed inside a black PolyVinyl Chloride (PVC) box, in order to be operated in dark conditions at a selected operating temperature. Each scintillator strip endorses two WLS fibers, as shortly detailed in Subsection 3.2, so that two SiPMs are required to read-out the light produced by the incoming muons, for a total number of 200 SiPMs for each detection module. A batch of about ten thousand SiPMs has been produced by STM and encapsulated into a Surface-Mount Device (SMD) optical package.

The technology spread in the SiPM breakdown voltage (V_{BD}) is less than 1 V, with a Gaussian mean value of 27.4 V and a standard deviation of 0.2 V, suggesting a good device uniformity within the tested batch.

Some of the final chips with the 4 SiPMs embedded were fully characterized. The SiPMs are biased and the output signal amplified by the use of a CAEN SP5600 general-purpose Power Supply and Amplification Unit (PSAU). The amplified signal is fed into a discriminator module, generating a logic output pulse each time a pulse crosses a predefined voltage level. A CAEN DT5720A fast digitizer (2 channels, 250 MS/s, 12 bit) allows to display the signals, evaluate the output charge of the sensor under test and measure its count rate in the absence of light [22].

The MUON-60 *DCR* as a function of the discriminator threshold V_{th} (also known as staircase curves) are reported in Fig. 4 at different overvoltage (V_{OV}) values.

SiPM absolute *PDE* measurements are carried out based on the photon counting method [22,23], by which the number of pulses per unit time in monochromatic light conditions are compared to the light level recorded by a reference NIST photodetector at the same time, and this process is then repeated for several wavelengths. *PDE* measurements in the 350–1000-nm wavelength

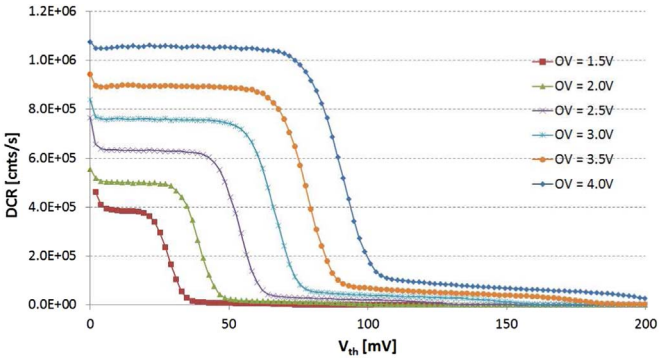

Fig. 4. Dark staircase curves of the MUON-60 detector as a function of the discriminator threshold, at different overvoltage values.

range are reported in Fig. 5 at three different overvoltage values, for a sample MUON-60 detector.

In the range 500–550 nm (which corresponds to the main emission spectrum of the WLS fiber) this device shows the highest *PDE* (with respect to other prototypes of the same series).

3.2. Read-out electronics

The output signals of the SiPM detectors are read by means of a specifically designed front-end circuits. A specific front-end case is realized for each module of the detector planes, in order to accommodate the SiPM detectors with related bias voltage, signal-processing electronics and temperature monitoring system. These front-end cases are suitably interfaced with the back-end acquisition electronics.

In consideration of the total number of functional modules required to achieve the desired space and angular resolution, an extremely large number of read-out channels are implemented for the whole muon detector. Therefore, a cost-effective compression technique is exploited within each module (100 strips), reducing the overall number of output channels to be processed by the front-end electronics and data acquisition system [27]. This is accomplished by the use of two WLS fibers running along the same strip (for a total of 9600 fibers, 200 per module) and connected to the same number of read-out SiPMs. Two WLS allow reading out of the scintillation light produced in a strip by means of two SiPM from one side only of the module. The time coincidence of the signals coming from two WLS of the same strip allow a strong reduction of spurious events, mainly due to the SiPM dark current.

For each detection module, 10 dedicated front-end boards (FEPMs) are designed and fabricated to host the 200 SiPMs and provide a versatile optical and mechanical interface with the WLS fibers. The 20 light signals arriving at each FEPM are sorted two-by-two in correspondence of each scintillator strip, producing 20 analog output pulses. Half of these signals (group signals, G_1-G_{10}) are connected in parallel in sets of five, and are then properly amplified and summed inside each board. All FEPMs of a single module are connected to a unique custom-made motherboard (CPM), where the remaining 10 amplified signals, one for each FEPM, are summed according to the same order in the FEPM boards (strip signals, S_1-S_{10}). Fig. 6 depicts a conceptual schematization of the adopted channel reduction approach. The S_i and G_i signals correspond, respectively, to the StripSet and the NeighSet Groups in [27].

Each of the FEPM boards (10 cm × 7 cm in size) hosts the SiPM devices, along with 13 fast operational amplifiers (THS3201, 1.8-GHz gain-bandwidth product), and an LM60 temperature sensor on the bottom layer to monitor the SiPM operating temperature on the board, useful to control each SiPM operating voltage with respect to temperature variations. A 30-pin Molex connector enables connection to the CPM motherboard, which provides the various supply voltages and processes the SiPM output signals. To allow oscilloscope testing of the boards, an output LEMO connector is also envisaged. Fig. 7 shows the schematic of the circuit of the FEPM board dedicated to the formation of one of the group signals. Fig. 8 illustrates the Printed-Circuit Board (PCB) of the realized FEPM. In total, 480 FEPM boards and 48 CPM boards are required for the 48 functional modules of the Muon Portal tracker, distributed in the four logical detection planes.

The simplified block diagram of the CPM motherboard is illustrated in Fig. 9. The 20 signals from each detection module (G_1-G_{10}, S_1-S_{10}) are compared to user-defined thresholds (TH_1-TH_{20}) produced by an integrated Digital-to-Analog Converter (DAC). Subsequently, the resulting digital pulses are stretched by monostable multivibrators (60-ns time width) to ensure proper adaptation and correct sampling of the signals. At the output of the monostable circuits, the digital pulses are buffered through dedicated line drivers to avoid signal losses due to the long wiring connection toward the back-end modules. Fig. 10 depicts the PCB of the realized CPM motherboard (80 cm × 7 cm dimensions).

The back-end programmable logic is based on a VIRTEX-II Field-Programmable Gate Array (FPGA) module, operating at 40 MHz and programmable through the LabView software. It allows to set the DAC thresholds, sample the digital pulses from each front-end module, decode the hit strips and produce a label frame for each event. The output data are pre-analyzed and stored into a data acquisition system. For the read-out of the four logical planes of the Muon Portal detector, 8 dedicated PXI-7813R boards,

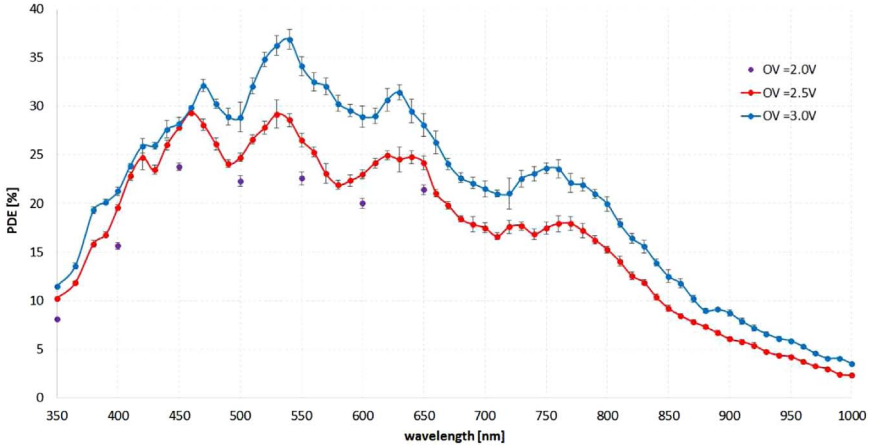

Fig. 5. Photon detection efficiency of the MUON-60 detector as a function of the light wavelength, at different overvoltage values.

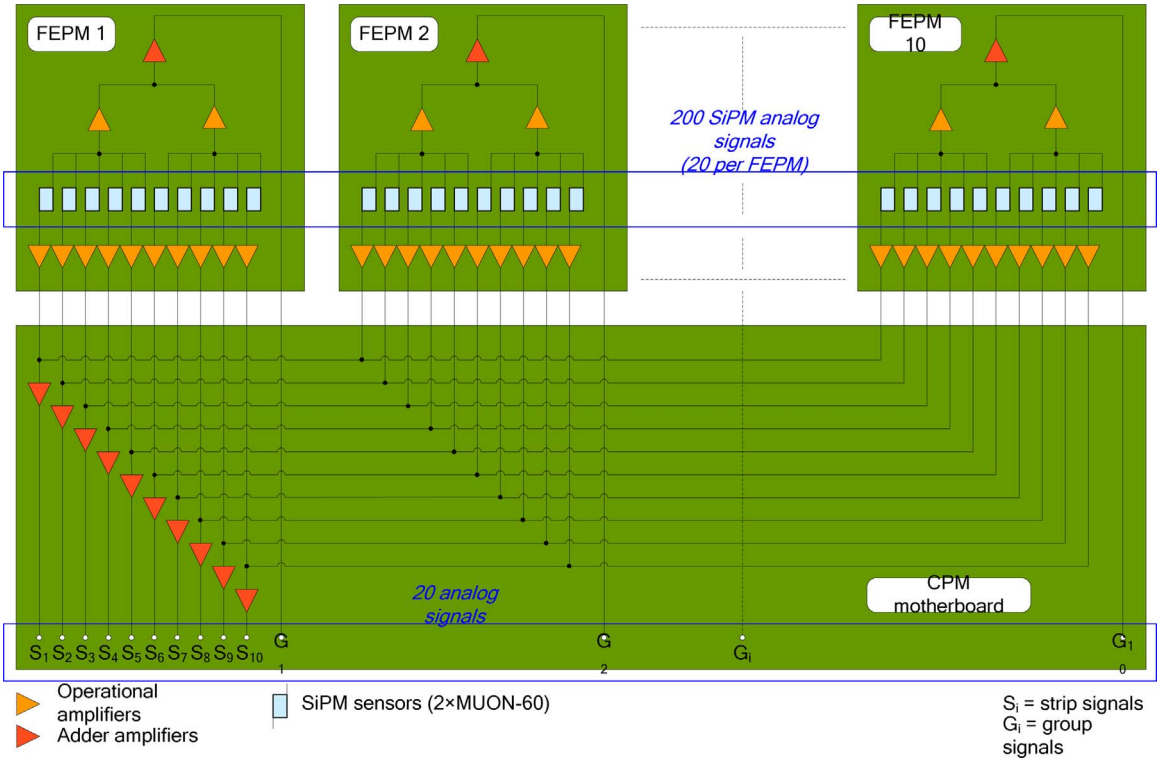

Fig. 6. Simplified schematization of the channel reduction strategy applied to a single detection module.

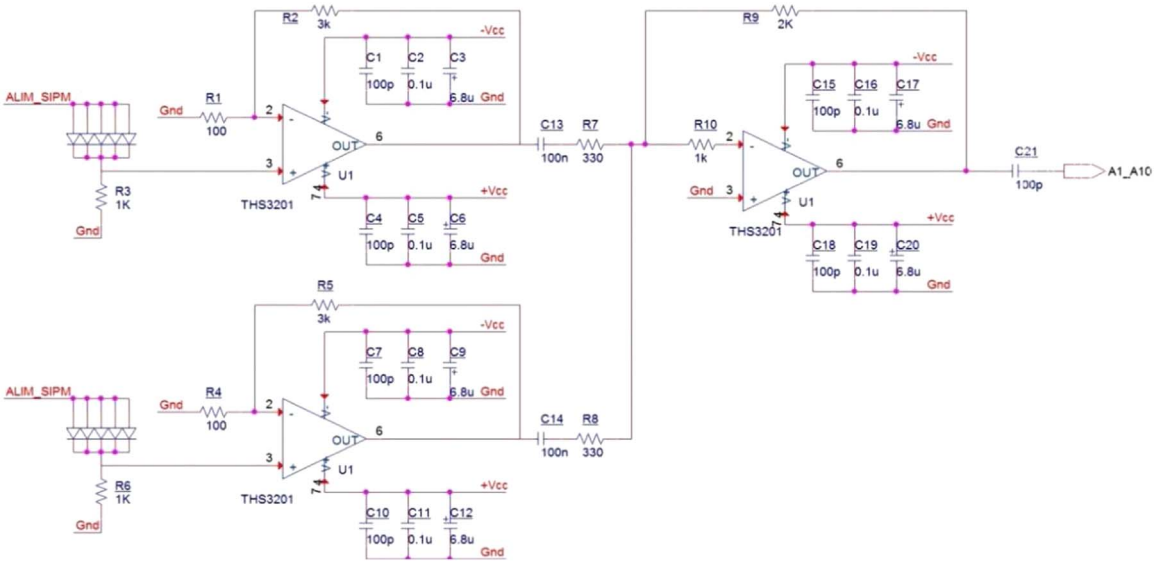

Fig. 7. Schematic of the circuit inside the FEPM board dedicated to the formation of one of the group signals.

provided by National Instruments, and a real-time calculation module (NI PXIe-8135) are used to correlate the signals from all detection planes, while a GPS device (NI PXI-6682), housed into a suitable crate, is also exploited for synchronization.

The use of SiPM photo-sensors to measure the signals coming from the WLS fibers, requires a remote adjustable power supply, able to compensate the variations of the intrinsic photo-sensor characteristics (gain, *PDE*, dark current) caused by the surrounding environment. To this purpose, the power supply section is provided with a software temperature controller, able to stabilize the working points of the SiPMs, which were suitably selected to have similar characteristics. In fact, as shortly described, the temperature monitoring and the setting of the SiPM operating voltage allow temperature variations to be compensated.

Moreover, to improve the uniformity of the SiPM response along the detection modules, the devices are subdivided into groups, depending on their breakdown voltage. SiPMs with similar characteristics are installed in the same detection module, in order to set, in groups of 200 SiPMs, the same bias voltage. In addition, thresholds are remotely controlled and automatically adjusted to account for possible gain variations.

Several calibration measurements are carried out in order to establish the most suitable SiPM single-photoelectron amplitudes by varying the photo-sensor operating voltage. Fig. 11 reports the

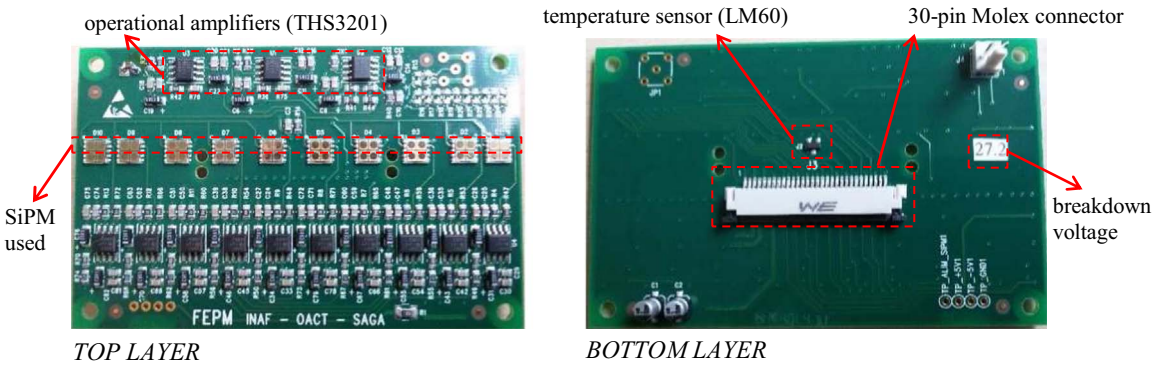

Fig. 8. PCB of the assembled FEPM board.

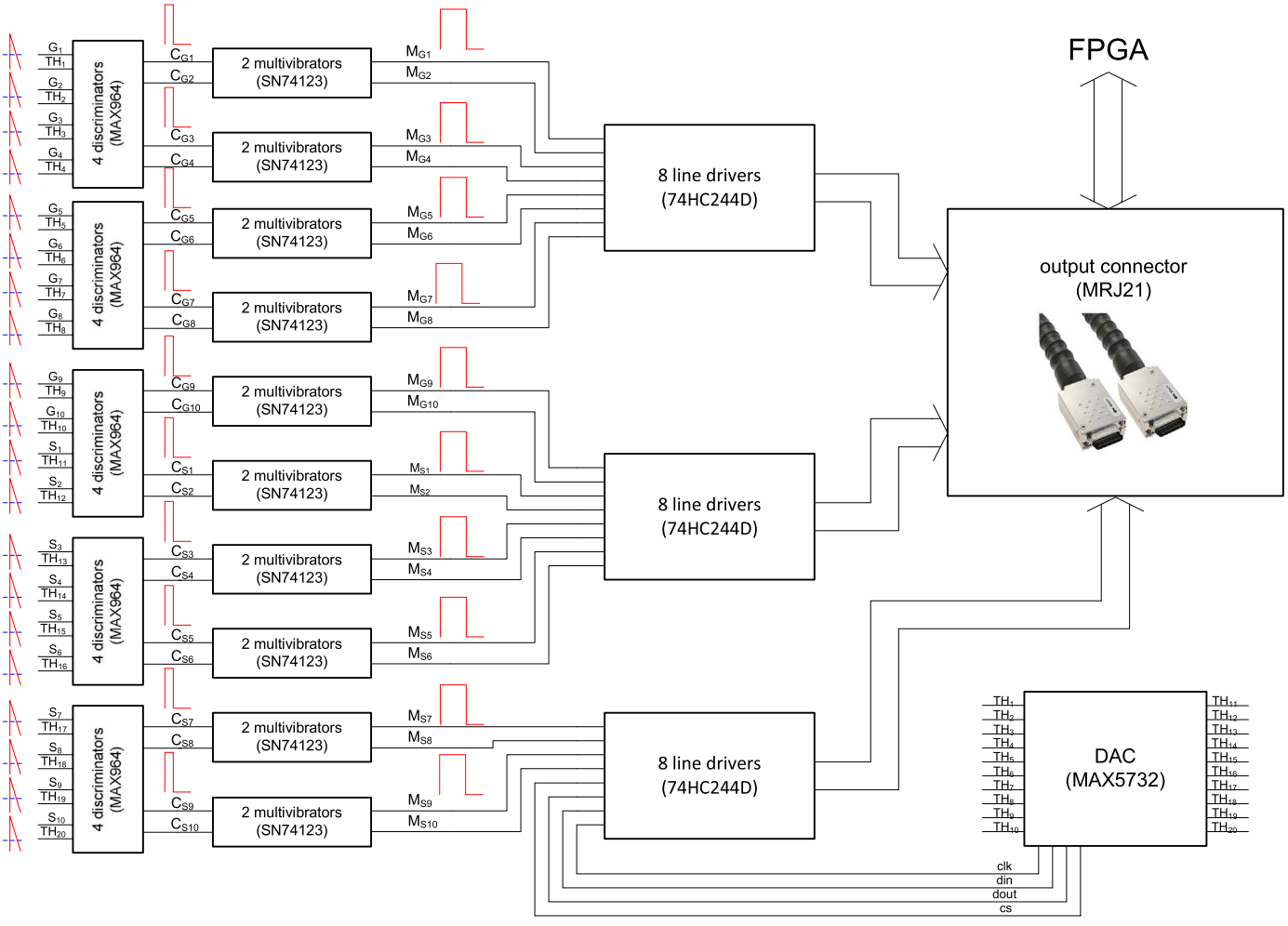

Fig. 9. Simplified block diagram of the CPM motherboard, showing its main building blocks.

oscilloscope measurements related to one of the 20 SiPM analog single-photoelectron pulses processed by the CPM motherboard, at four different overvoltage (V_{OV}) values, at 25 °C, and with the detectors kept in dark conditions.

As expected, a linear trend of the pulse amplitudes is obtained as a function of V_{OV}. The final bias voltage for the SiPM detectors is selected to ensure a 2.5-V overvoltage value, resulting from a reasonable trade-off between the SiPM dark count rate, from one side, and the SiPM single photo-electron amplitude (which must present adequate signal-to-noise ratio) and *PDE* from the other side.

As an exemplary illustration, Fig. 12 reports the captured waveforms related to one of the 20 SiPM analog signals, along with the resulting digital pulses at the discriminator and multivibrator outputs. In this case, a 50-mV threshold level is set by remotely programming the specific DAC of the CPM motherboard. A step width of about 60 ns is obtained for the digital signal, as expected, and this duration is established in order to guarantee a correct sampling by the back-end FPGA.

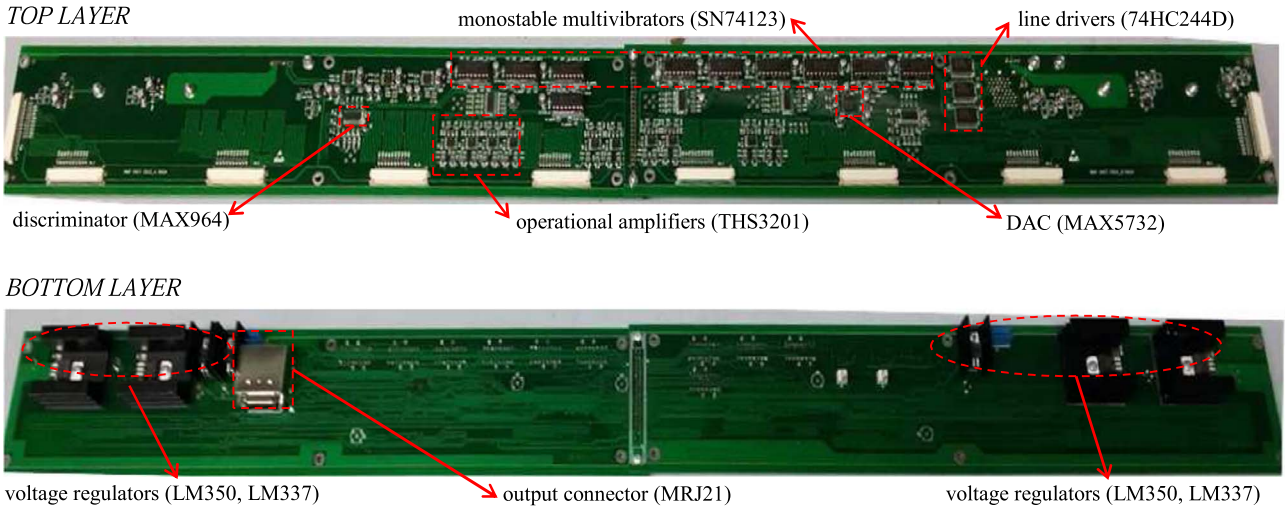

Fig. 10. PCB of the assembled CPM motherboard.

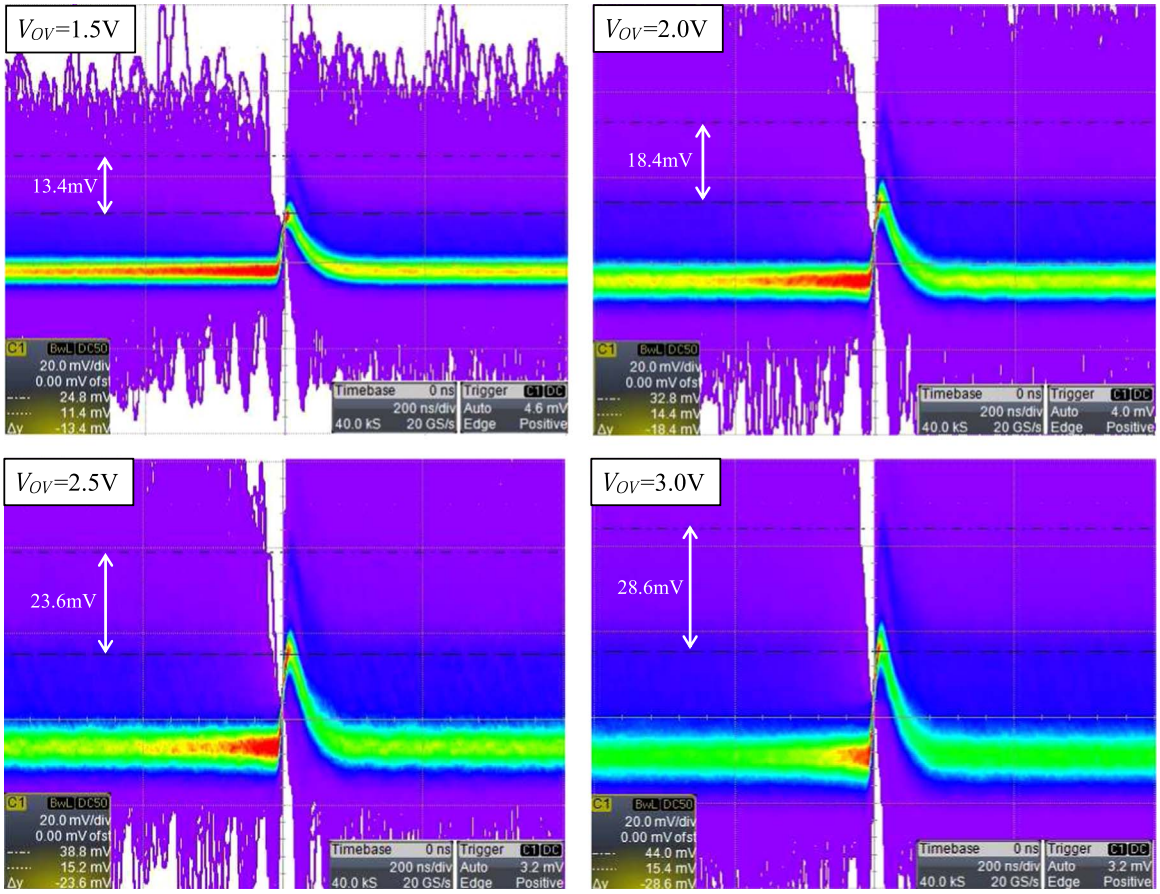

Fig. 11. Measurement results of the SiPM single-photoelectron amplitudes in dark conditions, at four different overvoltages, at 25 °C (V_{BD}=27.4 V).

4. Remote control system

Since the used photo-sensors require an adjustable power supply section to compensate for variations of the SiPM intrinsic characteristics, i.e. due to the temperature dependency of the SiPM breakdown voltage, an electronic module enabling monitoring of the SiPM temperatures and operating voltages is developed, also allowing remote programming of the SiPM bias voltages for SiPM gain stabilization.

The acquisition system for these housekeeping data relies on robust, feature-rich, and cost effective multi-channel analog input/output modules (ADAM 4015, 4017 and 4021 by Advantech[2]), using a controlled microprocessor integrating an ADC converter to turn Resistance Temperature Detector (RTD) signals and temperature sensor voltages into digital data, and a DAC converter to translate digital data set by the PC terminal into the desired SiPM

[2] http://www.advantech.com/products.

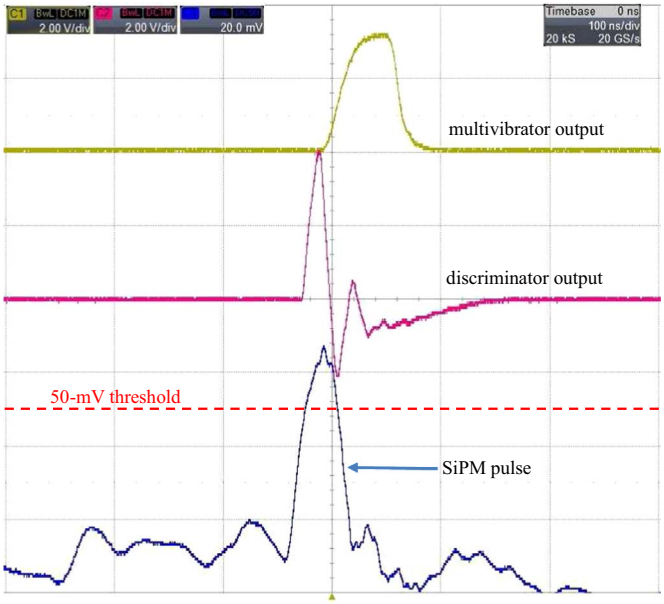

Fig. 12. Scope screenshot showing one of the 20 SiPM analog signals and the resulting digital pulses at the discriminator and multivibrator outputs.

analog operating voltages.

The acquisition system for monitoring and setting housekeeping data is schematically sketched in Fig. 14 for an entire logical detection plane. In particular, for each front-end electronics of a functional module, an ADAM 4015 device is used to read the temperatures provided by three PT100 sensors distributed along the front-end case; besides, an ADAM 4017 module monitors the output voltages of the LM60 sensors integrated in the FEPM boards (from which their temperatures can be achieved) and the SiPM bias voltage, whereas an ADAM 4021 unit is exploited to set the desired operating voltage for the 200 SiPMs.

As 48 front-end boxes are used for the entire Muon Portal, 144 ADAM devices are adopted in total and connected together through the so-called CAN-bus. The 144 ADAM modules allow to set 48 SiPM operating voltages and monitor 384 housekeeping data:

a) 144 temperatures coming from the PT100 sensors;
b) 192 temperatures coming from the FEPM boards;
c) 48 SiPM bias voltages.

Fig. 13 reports a schematization of the monitored and controlled parameters related to each of the 48 detection modules, that is, 3 temperatures read from the PT100 sensors through the ADAM 4015 device (2 inside the case and 1 outside the case), 4 temperatures read from the LM60 sensors through the ADAM 4017 device, and 1 voltage read from the ADAM 4017 via the connector in the CPM motherboard (monitoring the applied SiPM bias voltage). The SiPM bias voltage in each FEPM is set by the ADAM 4021 device through the CPM motherboard.

To manage remote housekeeping data communication over the Internet, an additional ADAM 4570 module is employed for encapsulating serial data and transporting it over Ethernet, guaranteeing compatibility with legacy serial devices and permitting remote control and backward software compatibility. An RS-485 multi-point serial connection allows to address each single device to receive and transmit data.

The high-level software communicating with the ADAM modules and enabling data acquisition sessions is implemented in Java language (version 1.8) using the NetBeans 8.1 Software Development Kit (SDK). The application is designed in order to guarantee the modularity of the detector architecture, and is able to elaborate data and manage controls.

Figs. 15 and 16 illustrate the program masks for the monitoring and control of housekeeping data. In particular, in the left panel of Fig. 15 the main interface is shown, enabling acquisition and accessing the data related to all single front-end modules of a logical plane. For each module, two checkboxes are envisaged both for data acquisition and for logging into external files. The central panel in Fig. 15, accessible by clicking on the relevant box button, allows to monitor the temperature detected by three PT100 sensors located inside the front-end case (TBox), along with four temperatures provided by the LM60 sensors embedded in the FEPM boards (TSiPM). Alarms are also managed and highlighted in red for those temperatures out of a specific range (over 40 °C and below 5 °C), implying anomalous sensor or cooling system operation. The housekeeping tab in the right panel of Fig. 15 shows the average temperatures of the LM60 sensors for each module, excluding inconsistent temperature values. Through the "Load" button of the mask in the left screenshot of Fig. 16, the SiPM operating voltages to be applied are loaded from a text file and visualized on the screen for each box of a logical plane. The "VSiPM on" button applies the set operating voltages to the SiPMs. The same overvoltage value is applied to the SiPMs in the same front-

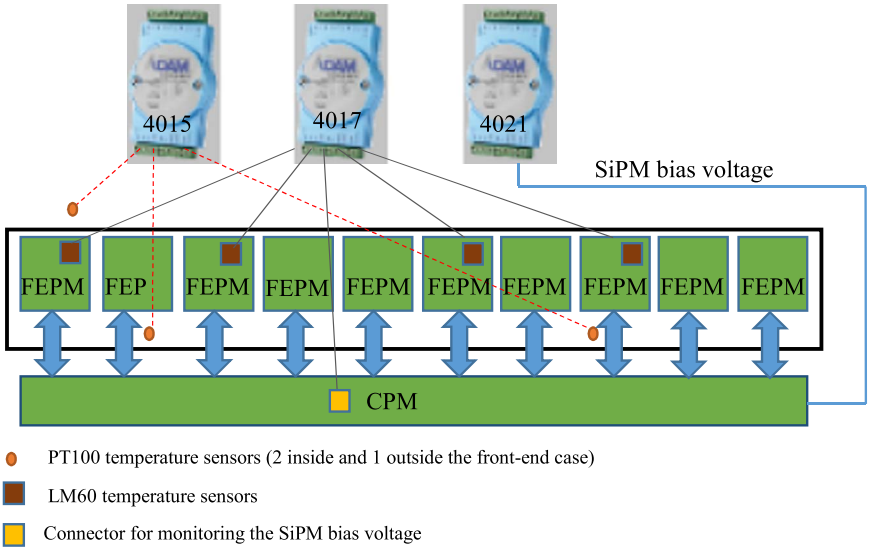

Fig. 13. Schematization of the monitored and controlled parameters for a single detection module.

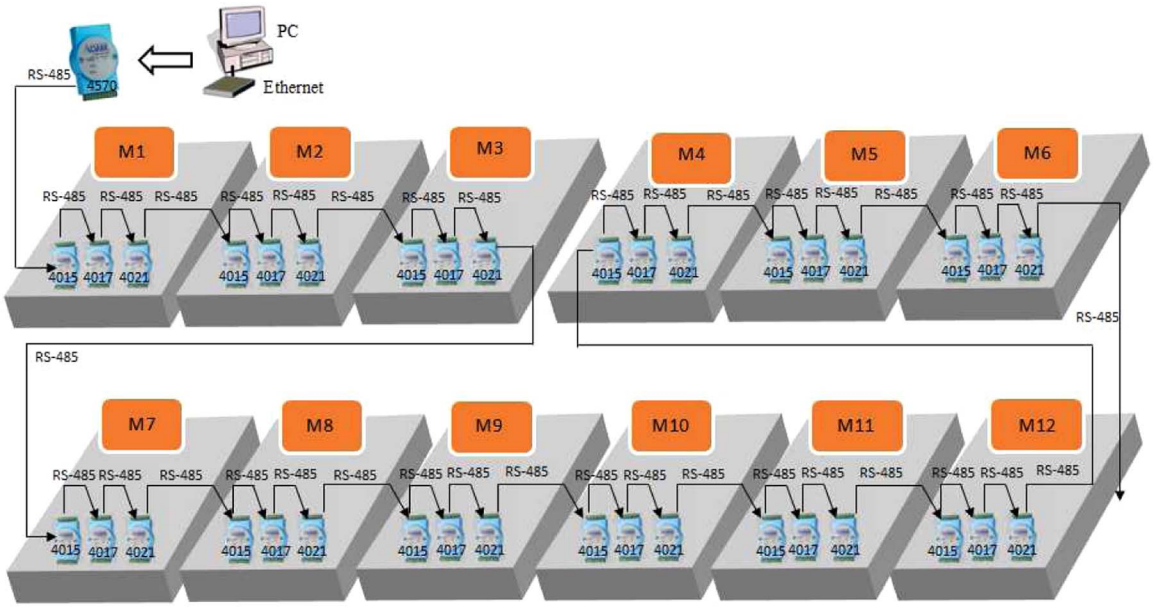

Fig. 14. Simplified block diagram of the acquisition system for the housekeeping data of a logical detection plane. In total, for each logical plane, 36 ADAM modules are employed.

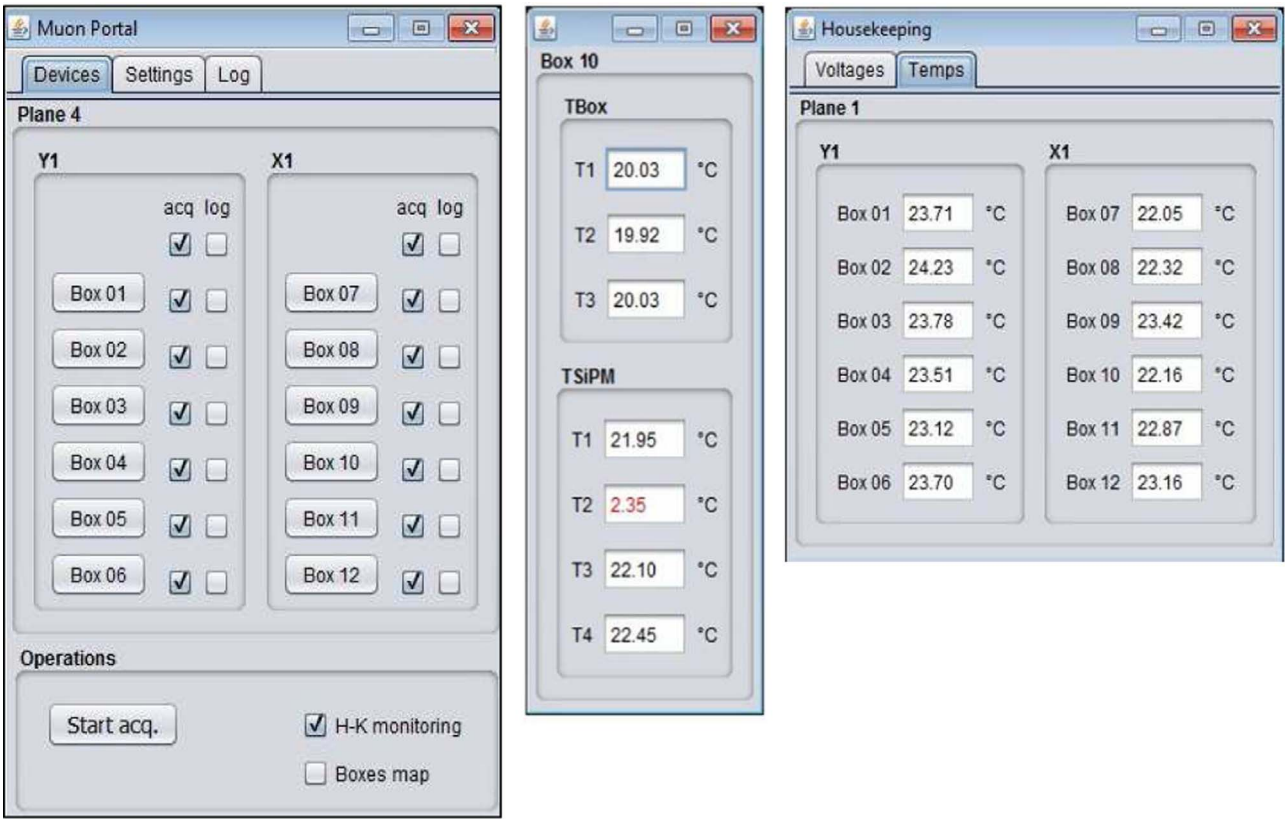

Fig. 15. Dialog windows of the implemented software for data acquisition. In the left panel, the main devices tab including the buttons accessing the single box and SiPM temperatures (central panel) of a logical plane. The right panel, shown by flagging the HK-monitoring checkbox in the main tab, depicts the average temperatures measured on the SiPM boards. Alarms are also managed and highlighted in red in the relevant pop-up window. (For interpretation of the references to color in this figure legend, the reader is referred to the web version of this article.)

end box according to the related breakdown voltage at 25 °C. An on-the-fly voltage adjustment is performed for all SiPMs of a whole logical plane. In addition, temperature compensation can be also accomplished, in accordance with the measured SiPM temperature coefficient (~32 mV/°C, resulting from the set-up and measurement methodology in [23]). In particular, the ADAM 4015 and 4017 devices read serially the housekeeping data of each module approximately every second (~48 s are required for reading the housekeeping data of the 48 detection modules). The four temperatures of the LM60 sensors in each module are averaged and the bias voltage of the related module is set by the ADAM 4021 device according to the following relationship

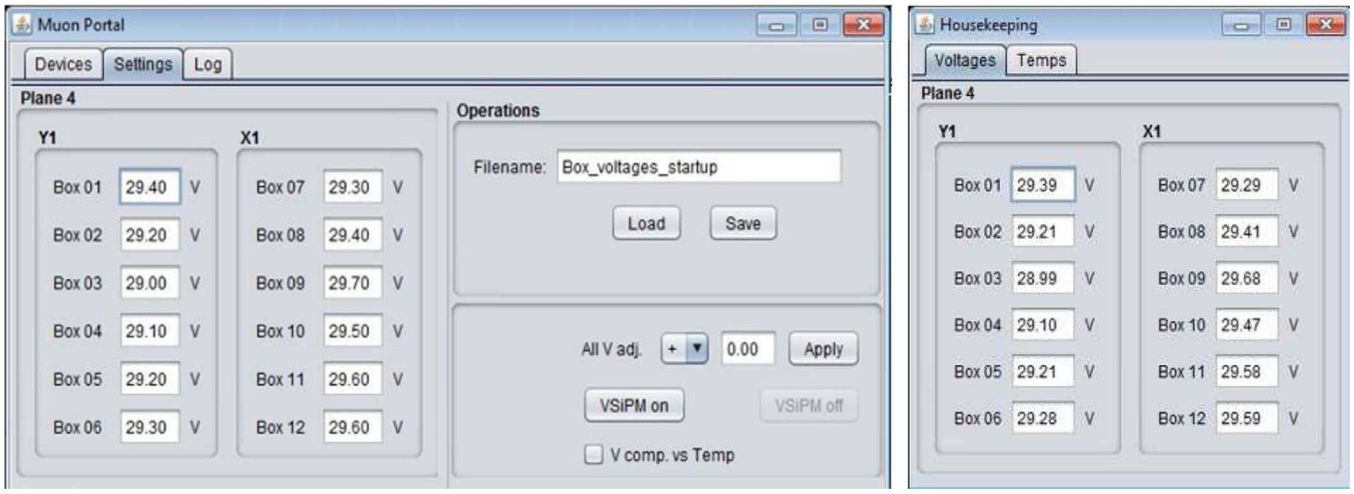

Fig. 16. On the left screenshot, setting window for the configuration of the SiPM operating voltages, including the checkbox for temperature compensation. On the right screenshot, SiPM operating voltages read on the CPM motherboard, very similar to the applied values.

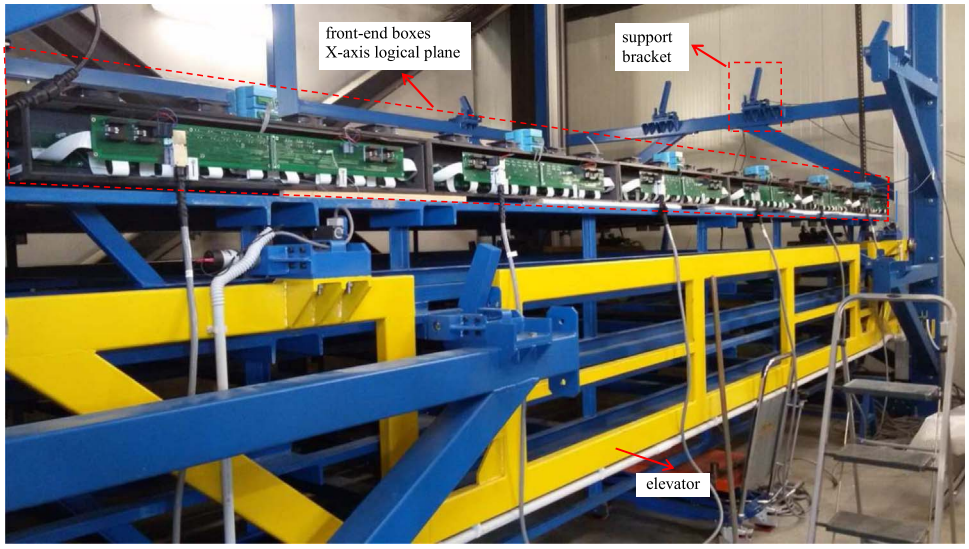

Fig. 17. Mechanical assembly of an entire logical *X*-axis logical plane, including 6 front-end cases with 6 CPM motherboards and 60 FEPM boards with related control system.

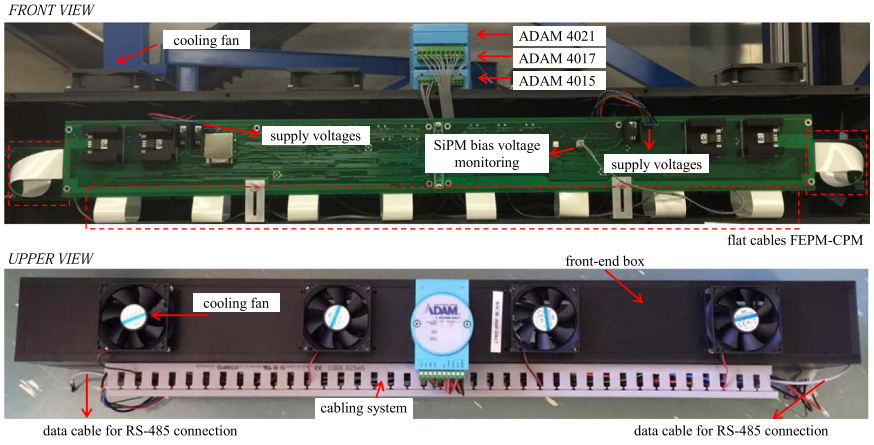

Fig. 18. Front and upper views of a single front-end case including electronics, control devices and cooling system for a whole detection module.

$$V_{BIAS}(T) = V_{BIAS}(25°C) + 32\frac{mV}{°C}(T - 25°C) \quad (1)$$

where T is average temperature of the four LM60 sensors, V_{BIAS} (25 °C) is the reference voltage at 25 °C, and V_{BIAS} (T) is the applied operating voltage which accounts for SiPM temperature compensation, in accordance with the estimated SiPM temperature coefficient.

In the right panel of Fig. 16, the applied SiPM operating voltages are monitored to inspect any possible deviations.

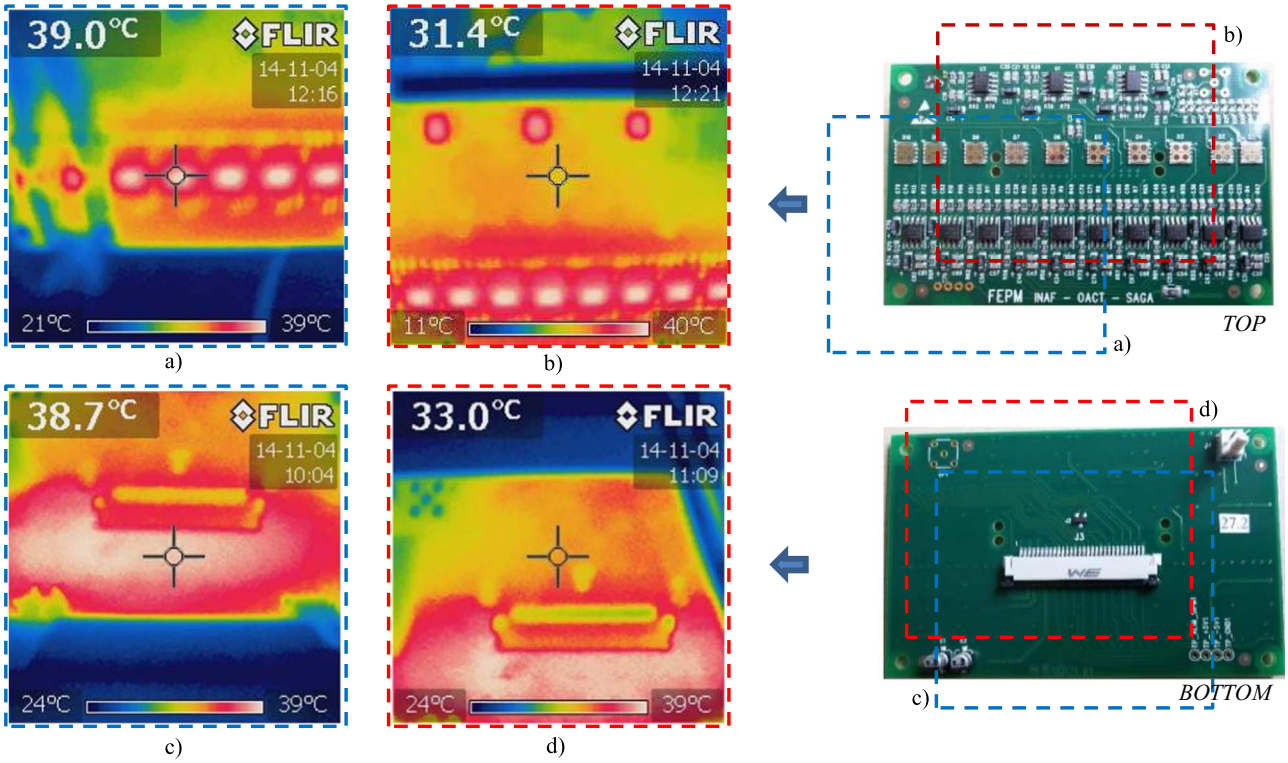

Fig. 19. Thermography of a FEPM board inside the front-end box, pointing at different locations: a) near the SiPM read-out preamplifiers (top); b) in close proximity of the SiPMs (top); c) near the SiPM read-out preamplifiers (bottom); d) in close proximity of the LM60 sensor (bottom).

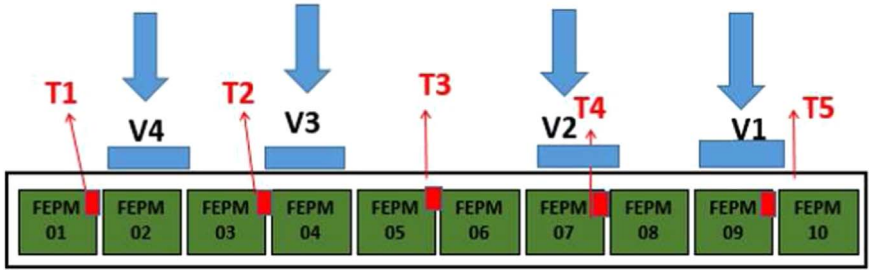

Fig. 20. Schematization of the temperature sensors distribution in a single functional module during thermic tests (five LM60 sensors integrated in the FEPM boards, and one external PT100 sensor close to the front-end case).

At software start-up, all parameters of the serial interface (number of port, data-bits, etc.), along with the SiPM operating voltage settings are shown in a dedicated "Log" text area retrievable from the specific tab of the main interface window.

5. Mechanical housing and cooling system

5.1. Mechanical structure

The bearing structure supporting the physical detection plans and the set of electrical and mechanical systems has been realized to ensure proper operation of all components, according to the technical specifications required. In particular, the mechanical design has been focused on the need to create a structure for an easy assembly and guarantee lightness and rigidity. The detector structure is made of carbon steel and is composed of horizontal shelves and beams supported by square-section columns. The modules, consisting of the scintillators in the *X* and *Y* directions, are sustained by appropriate supports, which are actuated at the moment when the plane is in its final (or defined) position; this is accomplished in a fully automated way and through a special

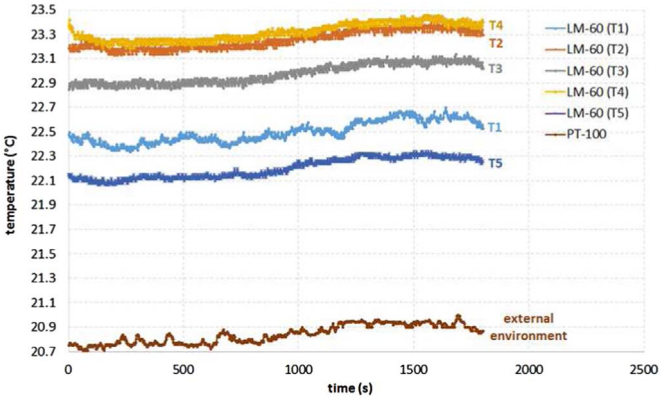

Fig. 21. Time evolution of the thermal curves related to a single front-end module during operation, showing a temperature difference of ~1 °C between the integrated LM60 sensors in a FEPM board.

system relying on linear guides. A system of sensors allows the monitoring of the correct positioning of the module and reports a possible anomaly. Fig. 17 reports a photograph of the mechanical

assembly of an entire *X*-axis logical plane, constituted by 6 front-end boxes with 6 CMP motherboards and 60 FEPM boards with related control system. One of the complete front-end modules is illustrated in Fig. 18, in both upper and front views, also showing the adopted cabling and cooling systems.

5.2. Cooling system

The main source of heat in the FEPM boards comes from the 13 THS3201 operational amplifiers, absorbing ~60-mW power each. On account of the compact dimensions of the FEPM boards, pulled together inside each front-end case, an efficient cooling system is required to dispose of the heat and provide the SiPMs with an optimal operating temperature.

Fig. 19 shows a few thermography screenshots of a FEPM board inside the front-end box, acquired when pointing at different locations of the board. The hottest temperature, as expected, is detected in close proximity of the THS3201 operational amplifiers on both sides of the board. As a consequence, the temperature of the SiPMs is strongly affected by their closeness to the amplifiers, so that an effective cooling system is required to provide SiPMs with an optimal operating temperature.

The front-end case being cooled has a convective flow of air moving over its surface, due to the combination of four fans which exchange heat with air. To ensure a uniform temperature inside the box, temperature measurements are carried out using five of the LM60 sensors in the FEPM and exploiting the acquisition system described in the previous section. Fig. 20 sketches the location of the temperature sensors (T1–T5) and cooling fans (V1–V4) used for testing the time evolution of temperature in one of the functional modules. An additional PT100 sensor is exploited to monitor the environmental temperature outside the front-end case.

The thermal curves as a function of time are depicted in Fig. 21 for a number of 1800 acquisitions. Each acquisition is determined by averaging 10 simultaneous temperature values. As shown, the combined effects and positions of the cooling fans allows a good temperature uniformity along the front-end case, with a maximal deviation of about 1 °C between the LM60 sensors. Thus, the SiPM temperature turns out to be only 3 °C higher compared to the external environment.

Control of the SiPM operating temperature is particularly important to keep the dark noise contribution restrained, thus allowing a good SiPM single-photoelectron resolution.

6. Conclusions and outlook

After an initial research and development phase and intense construction activity, the Muon Portal Project has entered its installation phase. The used SiPM photo-sensors and the developed front-end electronics have experimentally demonstrated the functionality of each detection plane installed. A large amount of simulations and tests on the detector planes are currently ongoing, allowing the tracking and testing of cosmic particles to be performed without the use of external scintillators. Due to the large acceptance of the Muon Portal detector for cosmic rays, complemented by a good angular reconstruction of the muon tracks and the possibility to discriminate electrons from muon events, this kind of detector is also foreseen to be employed for cosmic-ray scientific studies.

Acknowledgments

This work was financed by the Muon Portal Project and supported by the Muon Portal Collaboration, including both research centers (University of Catania, and INAF – Osservatorio Astrofisico di Catania) and industrial partners (ST-Microelectronics, Insirio, and Meridionale Impianti Welding Technology).

References

[1] E.C. Siciliano, et al., Comparison of PVT and NaI(Tl) Scintillators for Vehicle Portal Monitor Applications, Nucl. Instrum. Method. Phys. Res. A 550 (3) (2005) 647–674.
[2] E. Guardincerri, et al., Detecting special nuclear material using muon-induced neutron emission, Nucl. Instrum. Method. Phys. Res. A 789 (2015) 109–113.
[3] J.I. Kats, et al., X-Radiography of cargo containers, Sci. Glob. Secur. 15 (2007) 49–56.
[4] K.R. Borozdin, et al., Radiographic imaging with cosmic ray muons, Nature 422 (2003) 277–278.
[5] K. Gnanvo, et al., Imaging of high-Z material for nuclear contraband detection with a minimal prototype of a muon tomography station based on GEM detectors, Nucl. Instrum. Method. Phys. Res. A 652 (1) (2011) 16–20.
[6] S. Pesente, et al., First results on material identification and imaging with a large-volume muon tomography prototype, Nucl. Instrum. Method. Phys. Res. A 604 (2) (2009) 738–746.
[7] W. Priedhorsky, et al., Detection of high-Z objects using multiple scattering of cosmic ray muons, Rev. Sci. Instrum. 74 (10) (2003) 4294–4297.
[8] P. La Rocca, et al., Muon Portal Collaboration, Search for hidden high-Z materials inside containers with the muon portal project, J. Instrum. 9 (2014) C01056.
[9] F. Riggi, An extensive air shower trigger station for the muon portal detector, Nucl. Instrum. Method. Phys. Res. A 764 (2014) 142–149.
[10] S. Riggi et al., Muon Portal Collaboration, A large area cosmic ray detector for the inspection of hidden high-Z materials inside containers, in: Proceedings of the European Cosmic Ray Symposium (ECRS) 2012 Conference, Moscow, vol. 409, July, 2012, pp. 3–7.
[11] D. Lo Presti et al., Muon Portal Collaboration, A real time, large area, high spatial resolution tracker based on square scintillating fibers, in: Proceedings of the IEEE Nuclear Science Symposium and Medical Imaging Conference 2012 (NSSMIC), pp. 1244-1249, Anaheim, October, 2012.
[12] P. La Rocca, et al., Muon Portal Collaboration, Fabrication, characterization and testing of silicon photomultipliers for the muon portal project, Nucl. Instrum. Method. Phys. Res. A 787 (2015) 236–239.
[13] C. Pugliatti, et al., Muon Portal Collaboration, The muon portal double tracker for the inspection of travelling containers, IEEE Trans. Nucl. Sci. 62 (6) (2015) 3148–3154.
[14] V. Antonuccio et al., The muon portal project: development of an innovative scanning portal based on muon tomography, in: Proceedings of the IEEE Advancements in Nuclear Instrumentation Measurement Methods and their Applications (ANIMMA) 2013, Marseille, June, 2013, pp. 1–7.
[15] C. Petta, et al., Track reconstruction and VisIVO visualization of the cosmic secondary charged radiation paths in the detection of heavy nuclear materials using muon tomography, Astron. Soc. Pac. Conf. Ser. 461 (2012) 553–556.
[16] S. Riggi, et al., Muon tomography imaging algorithms for nuclear threat detection inside large volume containers with the muon portal detector, Nucl. Instrum. Method. Phys. Res. A 728 (2013) 59–68.
[17] M. Bandieramonte, et al., Automated object recognition and visualization techniques for muon tomography data analysis, in: Proceedings of the IEEE International Conference on Technologies for Homeland Security (THS), Waltam, USA, 2013, pp. 517–525.
[18] D. Marano, et al., Electro-optical characterization of MPPC detectors for the ASTRI cherenkov telescope camera, Nucl. Instrum. Method. Phys. Res. A 768 (2014) 32–42.
[19] V. Boccone et al., Characterization of new hexagonal large-area geiger avalanche photodiodes", in: Proceedings of the IEEE ANIMMA, 2013, pp. 1–6.
[20] P. Eckert, et al., Characterisation studies of silicon photomultipliers, Nucl. Instrum. Method. Phys. Res. A 620 (1) (2010) 217–226.
[21] H. Anderhub, et al., A novel camera type for very high energy gamma-ray astronomy based on geiger-mode avalanche photodiodes, J. Instrum. 4 (2009) P10010.
[22] G. Bonanno, et al., Characterization measurements methodology and instrumental set-up optimization for new SiPM Detectors - Part II: optical tests, IEEE Sens. J. 14 (10) (2014) 3567–3578.
[23] G. Bonanno, et al., Characterization measurements methodology and instrumental set-up optimization for new SiPM Detectors - Part I: electrical tests, IEEE Sens. J. 14 (10) (2014) 3557–3566.
[24] D. Marano, et al., Accurate analytical single-photoelectron response of silicon photomultipliers, IEEE Sens. J. 14 (8) (2014) 2749–2754.
[25] P. Buzhan, et al., Silicon photomultiplier and its possible applications, Nucl. Instrum. Method. Phys. Res. A 504 (2003) 48–52.
[26] S. Siefert, et al., Ultra precise timing with SiPM-based TOF PET scintillation detectors, in: Proceedings of the IEEE Nuclear Science Symposium Conference Records, 2009, pp. 2329–2333.
[27] D. Lo Presti, et al., OFFSET: optical fiber folded scintillating extended tracker, Nucl. Instrum. Method. Phys. Res. A 737 (2014) 195–202.